


## Sampling vacancy configurations with large relaxations using Smart Darting

D. Tanguy \*

Université Lyon, Université Claude Bernard Lyon 1, CNRS, Institut Lumière Matière, F-69622 Villeurbanne, France



(Received 2 October 2023; accepted 27 February 2024; published 18 March 2024)

Markov chain Monte Carlo simulations, combining the sampling of the position of the particles and their chemical nature, are very useful when calculating, for example, average site occupancies at crystalline defects in alloys. Unfortunately, when the relaxations around the solutes are large, the exchange moves can be systematically rejected because of atoms overlapping. As a consequence, the simulations are often trapped in nonphysical configurations. In this paper, the “Smart Darting” method from Andricioaei *et al.* is adapted and extended to propose a solution to this limitation. The method is tested in a particularly demanding case: the sampling of the arrangements of delocalized vacancies and divacancies in grain boundaries, both in the fcc and the bcc structure. Beyond the methodological aspects, intergranular vacancy clusters are interesting in several contexts, such as ductile fracture, irradiation, or thin-film dewetting, and therefore several properties have been measured that can be useful for mesoscale modeling: segregation energies, effective diffusion barriers in and out of the grain boundaries, vacancy-vacancy binding energies, and elastic dipole tensors.

DOI: [10.1103/PhysRevMaterials.8.033604](https://doi.org/10.1103/PhysRevMaterials.8.033604)

### I. INTRODUCTION

Vacancy clusters and voids, particularly at interfaces, are important in various contexts. They are at the origin of crack embryos in plasticity-related fractures: they form at dislocation boundaries during ductile fracture of pure metals [1,2] and at the interface between the matrix and persistent slip bands in the early stages of fatigue crack formation [3]. In the presence of interstitial solutes, they can also lead to the formation of bubbles. Miura *et al.* [4] have shown by microtensile testing of individual grain boundaries that a critical He bubble size and intercavity spacing, in the 5 nm range, can induce a transition from ductile fracture to intergranular brittle fracture, with a drop in fracture toughness. The phenomenon can be reproduced, to some extent, by atomistic simulations with voids only [5]. In the case of hydrogen embrittlement, the role of nanoscale bubbles is less obvious [6], but it was shown that submicron dislocation cells are formed along the brittle crack path [7,8], and nanoscale roughness was measured on the fracture surface [9]. Therefore, understanding how vacancies cluster along interfaces (cell walls and grain boundaries) under the influence of stress and temperature is important for modeling fracture in many different conditions.

Atomistic simulations are tools of choice, with their limitations, for addressing this question. Much has been learned about single vacancies in interfaces. In fcc metals, they diffuse preferentially along dislocation cores but also along the stacking fault ribbons. The activation energy is slightly reduced in comparison to the bulk [10–12], but the mechanism remains a simple vacancy-first neighbor exchange, i.e., the relaxations of the neighbors are marginal [11]. The situation is quite different in grain boundaries [13]. The relaxations

are often large, especially in the configurations of low energy (the most statistically visited), and to such an extent that the vacancies are said to be “delocalized” [14,15]. Furthermore, some grain boundary sites cannot host stable vacancies. This can lead to long diffusion jumps where several atoms are displaced [13,16]. At increasing temperature, the crystalline order within the core of the GBs is much lower than that in the bulk and continuously decreases until melting [13]. Stringlike cooperative motions of atoms, which are different from the long jumps at low temperature, are activated [17,18]. It was also shown that a grain boundary emerging at a free surface, which acts as a source of point defects (interstitials in this case), can transition with temperature between different structures. The reverse transformation could be obtained by absorbing vacancies [19]. More generally, it is well known that the construction of a grain boundary, defined by a set of macroscopic geometric parameters, requires the optimization of the energy with respect to microscopic parameters which are the relative translation of the two grains, plus the number of atoms within the interface [20]. Recently, not only the lowest-energy structures but also all metastable structures [21,22] were found. The structural unit model was generalized, and its ability to predict the stable and metastable structures of families of tilt boundaries, as a function of the misorientation angle, was established. The large number of these metastable structural units, and the quasicontinuous spectra of their excess energies, indicate that mixtures of such structures should exist at nonzero temperature. Since they can also have different numbers of atoms, the mixing of structural units could be an efficient way of accommodating vacancies. This is of particular interest for designing materials resistant to irradiation [23–26]. In this context, detailed studies of the absorption of vacancies were conducted in a fcc-bcc interface composed of a network of misfit dislocations. Delocalized vacancies were not found to attract each other, although misfit

\*dome.tanguy@univ-lyon1.fr

dislocation intersections constituted preferential segregation sites [25]. In addition, mixed tilt/twist GBs in Cu [26] were submitted to the absorption of large quantities of vacancies. The same GB core structures were visited periodically during vacancy loading when the GB changed structure by translation and shear. Both studies show that grain boundaries can be tolerant to large quantities of vacancies. Note that no void formation was found by molecular dynamics. In the bulk, experimentally, void formation appears when a critical vacancy concentration, in the range of  $10^{-2}$ , and at a high enough temperature, is reached [27]. Simple atomic kinetic Monte Carlo and simulations of phase demixion by atomistically informed Cahn-Hilliard equations can qualitatively reproduce the phenomenon [28].

Most of the valuable results summarized above have been obtained by molecular dynamics (MD). However, this method has well-known limitations, particularly concerning the limited timescale, which is somewhat compensated by working at high temperature. In this case, the grain boundaries are populated by defects, in addition to the vacancies deliberately introduced in the system. They complexify the analysis and influence the mechanisms that constitute unwanted side effects if the interest is in the low-temperature behavior. Few studies of interfacial vacancies use elaborate versions of MD [12,16], such as hyper-MD or temperature-accelerated dynamics, but these might suffer from a slowing down due to low barriers. These methods have evolved [29,30] and, combined with Adaptive Kinetic Monte Carlo (AKMC) [31,32], have successfully simulated the dynamics of vacancies in a thin slab, in particular the reentry of vacancies from the surface into the subsurface on the microsecond timescale [33]. Nevertheless, they might still be limited by the “low barrier” problem in the case of grain boundaries because of the transitions between structural units or by the massive number of transition searches necessary for AKMC. When only clustering tendencies are searched and not a realistic dynamics, Markov chain Monte Carlo, where the full phase space is sampled (i.e., site occupancies and relaxations), is very useful [34]. For example, in the semi-grand-canonical ensemble, it was used to study intergranular segregation [35,36]. Nevertheless, it suffers from the limitation of the vanishing acceptance rate of exchanges when relaxations around solutes are large, which is the case for delocalized vacancies.

In this context, we present a simulation methodology that overcomes the trapping issue of Markov chain Monte Carlo (MCMC). In the first part of the paper, the method is detailed and illustrated in the case of a vacancy occupying a peculiar GB site where it can be in two states: one localized and another delocalized. The power of the method is demonstrated as it succeeds in sampling, with a high acceptance rate, the occupancy of different crystallographically equivalent positions, in the delocalized state. Then, the average vacancy occupancies corresponding to the equilibrium between the GB site and a bulk site are calculated by exchange moves using two different paths: one going through the localized state and another going through the delocalized state. The energy barrier between the localized/delocalized vacancy states can be tuned by changing the strain perpendicular to the interface in such a way that the two states can be equilibrated by atomic displacement

moves only. In this condition, the occupancies calculated by the two different paths should be equal. This demonstrates that the method and its implementation are correct. In the second part of the paper, the method is used to study single vacancies and divacancies in four grain boundaries in Al (fcc) and in bcc Fe. The efficiency is measured, and the clustering tendency, which is quite different from one GB to another, is analyzed.

## II. MONTE CARLO METHOD

The method combines three aspects: the classical Monte Carlo simulation of the  $(N, V, T)$  ensemble by sampling the particles' positions [34], a periodic search for local energy minima, and finally transitions between these energy minima by the Smart Darting method [37]. In the following, each of these aspects is detailed. All throughout this section, the method and concepts will be illustrated by the example of a single vacancy in the core of the  $\Sigma 33(5\bar{5}4)[110]$  symmetrical tilt boundary, in Al, under strain.

### A. Localized/delocalized vacancies

The starting point is the classical Monte Carlo simulation of the  $(N, V, T)$  ensemble [34,38]. The definition of the microstates was modified to introduce vacancies [39]: the volume  $V$  is split into Voronoi cells according to the stable crystalline structure [Fig. 1(a)]. The  $N$  vectorial positions of the particles are replaced by  $N$  displacements with respect to the lattice nodes. It is implicitly considered that a Voronoi cell does not contain more than one particle. If this is not the case, the lattice should be refined by considering interstitial sites for example. The empty Voronoi cells are defined as vacancies. The set of  $N$  displacements is completed by a vector of  $M$  occupancies  $p_i$  such that  $p_i = 1$  if the site is occupied, zero otherwise, and  $M$  is the number of sites contained in volume  $V$ . If the system contains a grain boundary (GB), the lattice is the one of the minimum energy GB structure [40]. The configuration space is composed of the permutations of the vacancies (a swap of the occupancies) and of the volume of occupied Voronoi cells. The partition function to be sampled is

$$\mathcal{Q}_M(N, V, T) = \sum_{\{p_i\}^M} \frac{1}{\Lambda^{3N}} \int_{\text{vor}} d\vec{u}^N \times \exp(-\beta(\mathcal{H}(\{p_n\}, (\vec{u})^N))), \quad (1)$$

where “vor” is the volume of the Voronoi cell surrounding each lattice site,  $\Lambda$  is the thermal de Broglie wavelength [ $\Lambda = \sqrt{\hbar^2/(2\pi mk_B T)}$ ],  $m$  is the mass of the particle, and  $\hbar$  and  $k_B$  are the Planck and Boltzmann constants. The sampling is done by proposing random displacement increments to randomly selected particles (one particle at a time), provided the displacements remain within the Voronoi cells ( $\Delta u$  moves). In addition, swapping of occupancies between first neighbors (X moves) is also performed. For every elementary move, the energy variation is calculated and the move is accepted or rejected according to the Metropolis criterion. Most of the time, a particle remains confined to the vicinity of a lattice node. If a particle attempts to cross a facet of a Voronoi

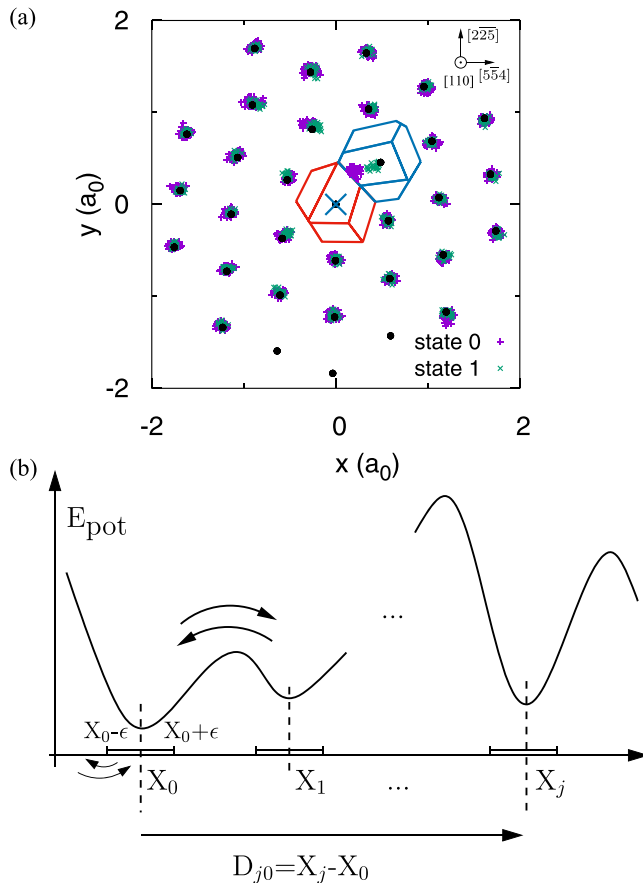


FIG. 1. (a) A collection of 84 microstates projected on the plane perpendicular to the tilt axis of the  $\Sigma 33(5\bar{5}4)[110]$  symmetrical tilt boundary, in Al, under 3% strain. Only the positions (small crosses) in the vicinity of the vacancy (large cross) and within two (220) layers containing the vacancy are shown. The black dots are the lattice sites (the edges of two Voronoi cells [41] are also shown). (b) Schematic illustration of the Smart Darting method.  $X_j$  is a local minimum of the potential energy, and  $\epsilon$  is the radius of the spheres around the minima.

cell towards a vacant site by  $\Delta u$  moves, the microstate is updated by swapping the site occupancies and modifying the displacements accordingly (vacancy displacements are zero). If the relaxations around the vacancies are small, this simple scheme is efficient [39]. Otherwise, the X moves are always rejected because of overlaps between particles.

For example, a collection of microstates obtained by the Monte Carlo procedure with  $\Delta u$  moves only is presented in Fig. 1(a). The lattice nodes are the black dots, while the crosses represent the position of the particles. The points within a packet grouped around a lattice node are from different microstates. Two Voronoi cells are also represented. One contains the vacancy (large cross) and is therefore empty regardless of the microstate. In the case studied, applying a strain creates additional minima in the energy landscape [see Fig. 4(a)]. It is illustrated by the second Voronoi cell, where the particles are split in two packets, each corresponding to one minimum. One of the packets is close to the lattice site [green crosses labeled “state 1” in Fig. 1(a)] and corresponds to the localized state of the vacancy. The other packet is far

from the lattice site (purple crosses labeled “state 0”) and corresponds to the “delocalized” state of the vacancy in the sense that if the packet was centered on the Voronoi cell border, the vacancy would be frequently attributed to one lattice site or the other as the neighbor switches cell by  $\Delta u$  moves. In addition, the transitions between states 0 and 1 occur at  $T = 300$  K by  $\Delta u$  moves only because the energy barriers between these states are low [0.1 eV/0.05 eV, Fig. 4(a)]. Vacancy/particle exchanges occur by X moves only, and only when the vacancy is localized. More precisely, starting the simulation with a microstate in the vicinity of state 0, the one of minimum energy, the simulation will attempt  $\Delta u$  moves with an acceptance rate of about 50% (the maximum amplitude of the displacements can be tuned) and will attempt also X moves. These will always be rejected because the exchange will introduce overlaps between particles. After several millions of accepted  $\Delta u$  moves, the system might be in the vicinity of “state 1.” Then an X move will be accepted and the vacancy will most likely move to a crystallographically equivalent site along the tilt axis, where the energy is the lowest. There, similar states 0 and 1 exist by translational invariance of the lattice along the tilt axis (these states will hereafter be called “topologies”). Then, the system will quit state 1 for state 0 after some  $\Delta u$  moves have been accepted because the barrier is low (0.05 eV). X moves will then be rejected again, and the vacancy will be trapped until the basin of attraction of state 0 is left again. Several concepts are introduced in this example that are useful for understanding the Smart Darting procedure adapted to vacancies: a “microstate” is a point (small volume) in configuration space, a “state” is a local minimum of the potential energy, the symmetries of the lattice (along the tilt axis) mean that there are rows of equivalent lattice sites favorable for the vacancy, and finally, the notion of “distance” between a microstate and a state. The sequence described is represented schematically in Fig. 1(b), where  $X_0$  and  $X_1$  are states 0 and 1, and  $X_j$  would be another state far away in configuration space, for example a state where the vacancy would be on a bulk site. The large curved arrows represent the transitions between  $X_0$  and  $X_1$  which require many  $\Delta u$  moves, and the small curved arrows represent the single  $\Delta u$  moves. They can bring a microstate in or out of the neighborhood of a state. These concepts will be reused to present the original Smart Darting method.

## B. The original Smart Darting method

Smart Darting [37] (SD) is an efficient way of avoiding trapping along the Markov chain. In the original method, a list of local minima of the potential energy  $\{X_i\}$  is known *a priori*. It can be obtained by MD or MC simulations at high temperature with periodic energy minimizations. The idea is to translate the system from one energy minimum to another while satisfying detailed balance. For this, the system cannot be transported directly at the energy minimum. The authors define “ $\epsilon$ -spheres”  $S_\epsilon(X_i)$  around each minimum by  $S_\epsilon(X_i) = \{X \mid \|X - X_i\| < \epsilon\}$ . In the one-dimensional (1D) example in Fig. 1(b), the spheres reduce to segments. They will be cubes intersected by Voronoi cells in the case of vacancies discussed below. The Monte Carlo procedure is a sequence of elementary moves. At each step, a random number is picked

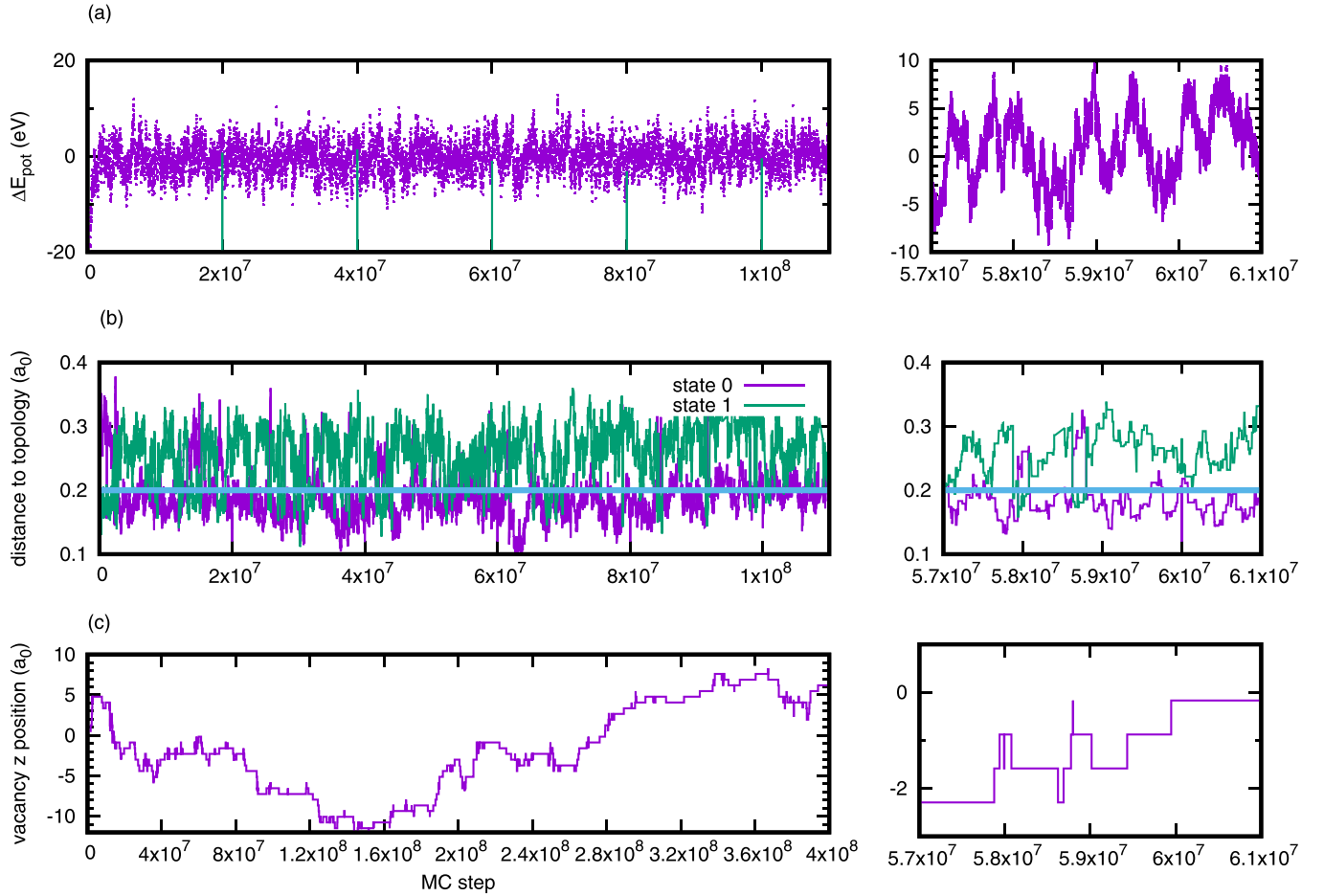


FIG. 2. Sampling of the configuration space of a system composed of the  $\Sigma 33(554)[110]$  symmetrical tilt grain boundary, under 3% strain with one vacancy. Temperature is 300 K and the model is Mishin's EAM for Al [42]. (a) Evolution of the energy (eV) as a function of the Monte Carlo steps, essentially because of  $\Delta u$  moves. Periodic energy minimizations are represented by vertical lines. (b) Evolution of the distance between the current microstate and states 0 (vacancy delocalized and on the most favorable GB site) and 1 (localized). The states are shown in Fig. 3. The Smart Darting parameter  $\epsilon$  is set to  $0.2a_0$ . As a consequence, the system is usually within the neighborhood of state 0 or 1, and therefore, the number of Smart Darting moves attempts is close to the maximum. (c) Evolution of the  $z$  position of the vacancy, illustrating acceptance of Smart Darting moves between the vacancy and one of its first neighbors along the tilt axis. The comparison of the zooms [right pictures (b) and (c)] shows that Smart Darting moves are accepted whether they are performed between states 0 or between state 0 and 1 at different  $z$  positions.

to decide, with fixed probabilities, which type of move will be attempted, either particle displacement or an SD move. If an SD move is picked, the procedure is (i) calculate the distance to every minimum and determine if  $X$  is within one of the  $\epsilon$ -spheres; (ii) if not, the current microstate is added one more time to the Markov chain; (iii) if  $X$  is within  $S_\epsilon(X_i)$ , pick at random another state  $X_j$ , calculate the “dart”  $D_{ji} = X_j - X_i$ , and add it to the current microstate, i.e.,  $X_{\text{new}} = X + D_{ji}$ . By this translation, the microstate remains at the same distance from the minimum, and since the volumes of the spheres are the same, the move is symmetric. The energy difference is calculated, and the acceptance/rejection by the Metropolis rule establishes detailed balance. Figure 1(b) illustrates the different ingredients: the small curved arrows are elementary displacement moves which enable sampling configuration space in the vicinity of  $X_0$  [in the sphere  $S_\epsilon(X_0)$ ], in and out of the sphere, and eventually bringing the system in the vicinity of other minimum  $X_1$  if the energy barrier between them is small], while dart  $D_{j0}$  translates the system from a microstate

in  $S_\epsilon(X_0)$  to another one in  $S_\epsilon(X_j)$ . This is particularly relevant in the case in which the barriers are too high to be crossed by a chain of elementary displacement moves.

### C. Adapting Smart Darting to vacancy clusters

The original method has to be adapted to the case of intergranular vacancies. In particular, the states cannot be determined by energy minimization from high-temperature MD or MC simulations because the vacancy clusters might not be stable at that temperature, or the vacancies might not even stay in the grain boundary. Furthermore, high temperature favors the mixing of different structural units [23,24], which would drastically increase the number the states. Instead, the list of states is constructed on the fly. In addition to the elementary MC moves, periodic energy minimizations are performed, i.e., the simulation is a series of cycles composed of a sequence of  $\mathcal{N}$  microsteps, typically 20 million, where moves are randomly picked between  $\Delta u$ ,  $X$ , and SD, followed by

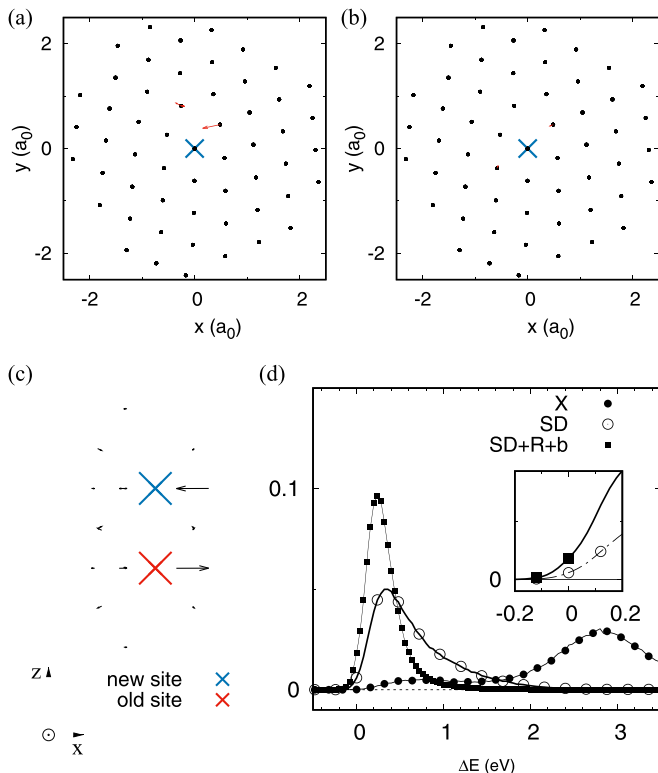


FIG. 3. Relaxations around a single vacancy (large cross) on the most favorable site of the  $\Sigma 33(554)[110]$  symmetrical tilt grain boundary, strained by 3% perpendicular to its plane. (a) State 0 (“delocalized vacancy”) and (b) state 1 (“localized vacancy”). Displacement values larger than  $0.05a_0$  are represented by arrows. They constitute, together with the site index, the topology used for the Smart Darting moves. (c) Vectors represent the “dart” for moving the vacancy along the tilt axis by one period. (d) Distribution of the energy variation  $\Delta E$  (eV) when a simple exchange (X), a simple Smart Darting exchange (SD), or a Smart Darting exchange plus the sampling of the neighbors, including the bias in the acceptance rule  $-kT \log \frac{\prod_{(n \rightarrow o)}(o \rightarrow n)}{\prod_{(o \rightarrow n)}(n \rightarrow o)}$  (SD + R + b) [Eq. (7)], is made. Only neighbors with a relaxation larger than  $0.1a_0$  were considered, and the acceptance rate was on the order of 5% at  $T = 300$  K.

an energy minimization and a search for states. At the end of the search, the list of states is enriched and a new sequence of  $\mathcal{N}$  microsteps is run, starting from the last microstate of the previous sequence. In other words, the minimized configuration is used only to enrich the list of states and does not appear in the chain of microstates. The cycles are illustrated by Fig. 2(a), where the potential energy is represented as a function of the number of MC microsteps. The vertical lines correspond to minimizations.

Furthermore, the goal is to use Smart Darting to perform single-vacancy–particle exchanges, and therefore the idea is to characterize the environment locally (particle relaxations and relative position of the other vacancies) around each vacancy of the system in the state under consideration. If the GB structure is periodic, there are many crystallographically equivalent favorable sites for a vacancy. Therefore, the local environment should be characterized in a way that is independent of which periodic cell the vacancies are in. This is obtained in the following way. The lattice sites of an elementary crystallographic

cell (for example, one “coincidence lattice” cell) are given an index. For each vacancy, the local configuration is defined by the index of the vacant site and the displacements  $\{\vec{u}\}$  of the neighbors, within a certain radius. These are referenced by the indexes of the site the neighbor occupies and the  $z$  position of the site, relative to the  $z$  of the vacant site, called  $\Delta z$ . The direction  $z$  is the direction of the tilt axis. The ensemble given by the index of the vacancy and the list of  $\{\text{index}, \Delta z, \vec{u}\}$  of the neighbors is called a “topology,” in reference to the kinetic-activation relaxation technique [32]. The process of transforming a site-specific collection of displacements into a local set of displacements relative to the position of the central vacancy is called “extraction of the topology.” The spatial domain over which  $\{\vec{u}\}$  is collected should be sufficiently large to contain all the sites that are significantly influenced by the presence of the vacancy. Otherwise, the vacancy-particle exchange attempts will be systematically rejected because of overlaps of particles. If the domain contains other vacancies, the topology also contains their index and  $\Delta z$ . Finally, a list of topologies is used in the Smart Darting move instead of a list of states, i.e., a list of local environments for vacancies (extracted from local energy minima). The “current topology” is also defined. It is the one extracted from the current microstate in the Markov chain.

The next modification to the original SD method is the definition of the  $\epsilon$ -sphere. In the MC algorithm, the SD move starts by selecting a vacancy at random. The lattice site it occupies is labeled  $i$ . The current topology centered on  $i$  is “extracted” from the microstate. Then the distance between the current topology and the  $k$ th compatible topology of the list ( $\text{dist}_k$ ) is

$$\text{dist}_k = \max_{(\text{index}, \Delta z)} \{|u_l^k - u_l|\}_{l=x,y,z}, \quad (2)$$

where  $u_l^k$  is the  $l$  component of the displacement of the site “index” at  $\Delta z$  from site  $i$  of the topology  $k$ , and  $u_l$  is the same but in the current topology. Topology  $k$  is compatible with the current topology if, locally around  $i$ , the vacancies are distributed in the same way, i.e., same index and  $\Delta z$ , including the central vacancy. An  $\epsilon$ -sphere is defined by  $\text{dist} < \epsilon$ . It is a collection of cubes of side  $2\epsilon$  centered on the position of the neighbors of the vacancy, in the configuration of local minimum energy.  $\text{dist}_k$  can be large as soon as a neighbor has a displacement significantly different from the one it has in topology  $k$ . Figure 2(b) shows the evolution of the distance to the topologies extracted from the states 0 and 1 of Fig. 1(a). The distance can be larger than  $0.3a_0$ . This occurs when one neighbor is close to the side of its Voronoi cell when the microstate is in the basin of attraction of state 0 [Fig. 1(a)]. In this case, the distance to topology 1 (localized vacancy) is large. Other details concerning  $\epsilon$  are mentioned in Appendix A.

Finally, a “dart” is defined. If there exists a topology  $k_i$  where  $\text{dist}_{k_i} < \epsilon$ , then the vacancy at  $i$  can be moved to another site by an SD move. For that, a site  $j$ , neighbor of  $i$ , is selected and a new topology is selected in the list of topologies (compatible with site  $j$  being occupied by a vacancy), referenced by  $k_j$ . The “dart” is then the combination of the swap of the occupancies of the lattice sites  $j$  and  $i$  and the translation  $\{\text{index}, \Delta z, \vec{u}^{k_j} - \vec{u}^{k_i}\}$ .

An example is given in Fig. 3, where (a) and (b) are the topologies extracted from states 0 and 1 [Fig. 1(a)]. The displacements are represented by arrows. Most of them are smaller than the size of the dots, which represent the lattice sites. The remarkable displacement already discussed several times is visible on topology 0. Imagine an SD move that shifts the vacancy by one period along the tilt axis while it is in the vicinity of topology 0 on the old lattice site and remains in the vicinity of topology 0 on the new lattice site. The corresponding dart [Fig. 3(c)] is  $-\vec{u}^0$  centered on the old vacant site and  $+\vec{u}^0$  centered on the new vacant site, where  $\vec{u}^0$  is given in Fig. 3(a). A one-dimensional random walk of the vacancy along the tilt axis is obtained [Fig. 2(c)] instead of a trapping on a single site. The simulation also contains topologies that would let the vacancy escape from the grain boundary, but this does not occur during this simulation at 300 K (the escape at 400 K is illustrated by a figure in the Supplemental Material [43]).

#### D. Construction of the topology list

So far, the way the states are searched has not been completely described. Starting the simulation with an empty list of topologies, the Markov chain is constructed with  $\Delta u$ , and X moves alone and is quickly trapped in a configuration where the vacancy is delocalized. At the end of the first cycle, the first topology is extracted. With only one topology, the SD moves are limited to proposing only one type of exchange, and only 1D random walks along the tilt axis are possible. Therefore, in addition to the extraction of the current topology, a series of robust nudged elastic band (NEB) calculations [44] between the current configuration and the ones obtained by swapping the vacancy with one of its neighbors (within the same range as the one for the SD move, which is not necessarily limited to first neighbors) is performed. If the NEB finds an intermediate configuration, the corresponding topology is extracted. Otherwise, the topology is extracted from the end point of the NEB. Therefore, the topologies are more than simple arrangements of vacancies over the lattice nodes because the same set of occupancies can lead to different relaxations. These topologies are stored, if unknown previously, in the list of known topologies and marked as “unsearched,” meaning that if they are visited and occupied during a future energy minimization, they should be searched for new transitions. In addition to topologies, the NEB gives energy barriers that are not exploited by the method, at the moment, but which constitute kinetic information that could be useful either to evaluate at which temperature the transitions could be realistic, or to open the possibility for kinetic Monte Carlo with a fixed catalog of rates collected during the MCMC simulation. It can be stressed that the MCMC simulation gives more accurate site occupancies than the ones the KMC simulations (with the catalog mentioned above) would give because anharmonic effects are included and also because the  $\Delta u$  moves participate in the exploration of configuration space, i.e., states that are not accessible to SD moves because the corresponding topologies are not on the list can be visited by  $\Delta u$  moves if the energy barriers to reach them are low enough.

#### E. Boosting the acceptance rate

In the example presented in Fig. 2, the acceptance rate is 0.7% for first-neighbor exchanges, by SD moves only, between equivalent sites along the tilt axis, in topology 0 (the one with the most extended relaxations). The distribution of the energy variation for SD moves is shifted by almost 3 eV toward low energies in comparison to the distribution for X moves [empty/full circles in Fig. 3(d)], which confirms that the problem of the overlap of the particles is solved. Nevertheless, there are few attempts that have a negative energy (see the inset). One way of improving the acceptance rate is to sample the positions of the particles that are significantly displaced from the lattice nodes during the SD move. For this, the “configurational-bias” Monte Carlo method [34,45] for growing chain molecules in dense systems has been adapted to the vacancy problem. Originally, a molecule is grown segment by segment by picking the segment’s orientation out of  $k$  trial orientations. The energy variation related to each trial orientation is calculated, and the new orientation is selected according to its Boltzmann weight in the list of trial orientations. It is clear that the probability of selecting this orientation is not random and depends not only on the environment (the configuration of the other molecules in the system), but also on the orientation of the segments previously grown. This probability must be introduced in the acceptance rule, and therefore it must be calculated both for the forward and reverse moves. This means, in the chain molecule example, that the old configuration has to be regrown segment by segment. In the case of vacancy exchange, the same procedure is followed, but instead of choosing orientations for segments, displacements are chosen for neighbors. This is done after the SD move is applied. A list of neighbors with significantly large “darts” is established, typically displacements larger than  $0.05a_0$ .  $Nn$  is the number of such neighbors. The displacements in the “old” configuration are stored as  $u_i^{\text{old}}$  to calculate the probability of the reverse move.  $i$  refers to the position of the neighbor on the list. Then, sequentially, the “new” displacement for every neighbor  $u_i^{\text{new}}$  is chosen among  $Nr$  random possibilities  $u_{ik}^n = r_k \epsilon + u_i^0$ .  $r_k$  is the  $k$ th random vector of the list of length  $Nr$ , and  $\epsilon$  is the size of the domain around the component of the dart  $\vec{u}_0$  on site  $i$  named  $u_i^0$ . The energy variation for every one of these trial positions is calculated and named  $\Delta E(u_{ik}^{\text{new}})$ . The probability of picking a displacement, for example  $u_{ik'}^{\text{new}}$ , on the list is

$$p(u_{ik'}^{\text{new}}) = \frac{e^{-\Delta E(u_{ik'}^{\text{new}})/kT}}{\sum_{k=1}^{Nr} e^{-\Delta E(u_{ik}^{\text{new}})/kT}}. \quad (3)$$

Once this is done, the index  $k'$  is dropped, and after all the neighbors have been treated, the energy of the new configuration is

$$E_{\text{new}} = E_{\text{old}} + \Delta E_{\text{SD}} + \sum_{i=1}^{Nn} \Delta E(u_i^{\text{new}}) \quad (4)$$

and the probability of choosing this set of displacements is

$$\prod_{i=1}^{Nn} (o \rightarrow n) = \prod_{i=1}^{Nn} p(u_i^{\text{new}}) = \frac{e^{-\sum_{i=1}^{Nn} \Delta E(u_i^{\text{new}})/kT}}{\prod_{i=1}^{Nn} \sum_{k=1}^{Nr} e^{-\Delta E(u_{ik}^{\text{new}})/kT}}. \quad (5)$$

The following is done for the reverse move: starting from the “new” configuration, the SD move is reverted and then, for each neighbor,  $Nr - 1$  displacements are selected at random within the  $\epsilon$  volume around the displacement corresponding to the reversed dart. The corresponding energy variations are calculated and named  $\Delta E(u_{ik}^{\text{old}})$  and the one for the stored “old” displacement  $u_i^{\text{old}}$  is named  $\Delta E(u_i^{\text{old}})$ . The probability that the old configuration is recovered during the reversed move is

$$\prod(n \rightarrow o) = \frac{e^{-\sum_{i=1}^{Nn} \Delta E(u_i^{\text{old}})/kT}}{\prod_{i=1}^{Nn} (e^{-\Delta E(u_{ik}^{\text{old}})/kT} + \sum_{k=1}^{Nr-1} e^{-\Delta E(u_{ki}^{\text{old}})/kT})}. \quad (6)$$

Detailed balance gives the acceptance rule:

$$\frac{\text{acc}(o \rightarrow n)}{\text{acc}(n \rightarrow o)} = \frac{\rho_n \prod(n \rightarrow o)}{\rho_o \prod(o \rightarrow n)} = e^{-[\Delta E_{\text{SD}} + \sum_{i=1}^{Nn} \Delta E(u_i^{\text{new}})]/kT} \frac{\prod(n \rightarrow o)}{\prod(o \rightarrow n)}. \quad (7)$$

By construction,  $\Delta E(u_i^{\text{new}})$  tends to be negative, on average. Therefore, in Eqs. (4) and (7), the energy variation related to the SD move,  $\Delta E_{\text{SD}}$ , tends to be decreased by  $\sum_{i=1}^{Nn} \Delta E(u_i^{\text{new}})$ , and therefore the acceptance rate increased. The term  $\frac{\prod(n \rightarrow o)}{\prod(o \rightarrow n)}$  is complex. Statistics about its distribution have been acquired numerically. It strongly depends on the number  $Nn$  of neighbors involved, with a strong tendency to degrade the positive influence of  $\sum_{i=1}^{Nn} \Delta E(u_i^{\text{new}})$ , to an extent where the acceptance rate could be lower than SD moves alone. The strategy followed consists in selecting the neighbors that are the most displaced during the SD move, keeping the number of neighbors low. For example, in the case of Fig. 3, a threshold of  $0.1a_0$  on the displacements leads to only four neighbors involved in the “configurational-bias” procedure. For  $N_r = 1000$ , the acceptance rate is 5%, i.e., a boost by a factor of 7 with respect to SD moves alone [empty circles/filled cubes in Fig. 3(d)]. With a threshold of  $0.05a_0$  and 10 neighbors involved, the acceptance rate is only 1.7%. With four neighbors, the total computational time of the SD move is only multiplied by a factor of 2 (using six threads).

### F. Validation

Finally, the question of the validation is addressed. The energy variation between states 0 and 1 (Fig. 3) is shown in Fig. 4(a). The barrier tends to zero when the strain goes to zero, i.e., state 1 [replica 0 in Fig. 4(a)] is unstable. The barrier is low enough to be crossed by  $\Delta u$  moves only, provided the temperature is high enough. The validation test consists in putting states 0 and 1 in equilibrium with a bulk site by two different paths, using two different MC moves. Path 0 is bulk  $\rightleftharpoons$  state 0  $\rightleftharpoons$  state 1, with the first equilibrium established by SD moves and the second by  $\Delta u$  moves. Path 1 is bulk  $\rightleftharpoons$  state 1  $\rightleftharpoons$  state 0, with the first equilibrium established by X moves and the second by  $\Delta u$  moves. The X moves have a nonzero acceptance rate because the neighbors are only weakly relaxed toward the vacancy. Figure 4(b) shows that the two paths lead to the same average occupancies, which establishes that the SD moves, including the configurational bias, are properly implemented.

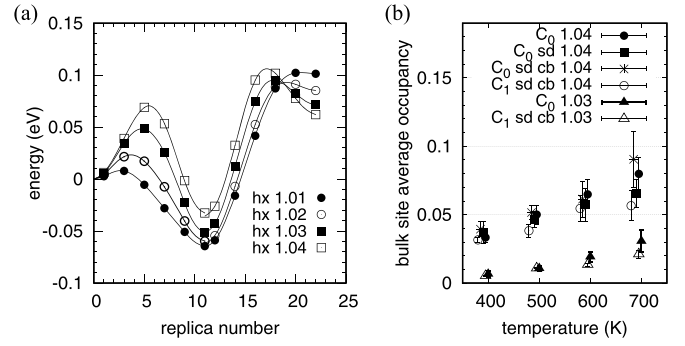


FIG. 4. (a) Energy profile between state 1 (replica 0) and state 0 (replica 11) obtained by the NEB, as a function of the homothety factor applied perpendicular to the GB. (b) Occupancy of a bulk site when it is put in equilibrium with the GB either in state 0 or in state 1, as a function of temperature and for two strain levels  $hx = 1.03$  and 1.04.

### III. APPLICATION TO DIFFERENT GRAIN BOUNDARIES

The method is applied to four symmetrical tilt grain boundaries, two in Al:  $\Sigma 33(554)[110]$  [46] (without strain) and  $\Sigma 13(320)[001]$  [47,48], and two in bcc Fe:  $\Sigma 29(730)[001]$  and  $\Sigma 9(1\bar{1}4)[110]$  [49]. The technical details are given in the Appendix B. The grain boundary structures, vacancy segregation energies (the profiles are in the Supplemental Material [43]), and relaxations when the vacancy occupies the most favorable position are shown in Fig. 5. The amplitude of the relaxations ( $u_{\text{max}}$  in Table I) is large: between  $0.1a_0$  and  $0.4a_0$  depending on the grain boundary. The efficiency of the Monte Carlo method is evaluated by measuring the acceptance rate for vacancy-particle exchanges in the different structures. To mimic diffusion, exchanges with nearest neighbors were proposed first. When the tilt axis is not aligned with a nearest-neighbor pair, the move involves leaving the site that is most favorable energetically and therefore the acceptance is biased by the change in segregation energy. Taking into account this effect, the list of neighbor sites is extended beyond the first neighbors to include the sites that are crystallographically equivalent, along the tilt axis. This means second neighbors for the [100] axis and third neighbors for the [110] axis of the bcc structure. The acceptance rate is measured specifically for moves that do not involve changes in segregation energy. Different degrees of complexity were tested. They are designated in Table I as X for the simple exchange, SD for “Smart Darting” alone, and SD + R + b for a Smart Darting exchange combined with a Rosenbluth sampling “R” of neighbor’s displacements and inclusion of the corresponding energy bias “b” in the metropolis criterion according to Eq. (7) [ $\Delta E_{\text{SD}}$  is the energy variation related to SD,  $\sum_{i=1}^{Nn} \Delta E(u_i^{\text{new}})$  to “R,” and  $-kT \log \frac{\prod(n \rightarrow o)}{\prod(o \rightarrow n)}$  to “b”]. The reported acceptance rate for the X moves only reflects the absence of acceptance after a large number of trials because of the relaxation of the neighbors shown in Fig. 5. The acceptance rate for SD moves is already very significant: between 1% and 6% depending on the structure. It can be improved up to between 3% and 10% by the SD + R + b move (Table I). As already mentioned above, the number of neighbors ( $Nn$ ) involved in R sampling

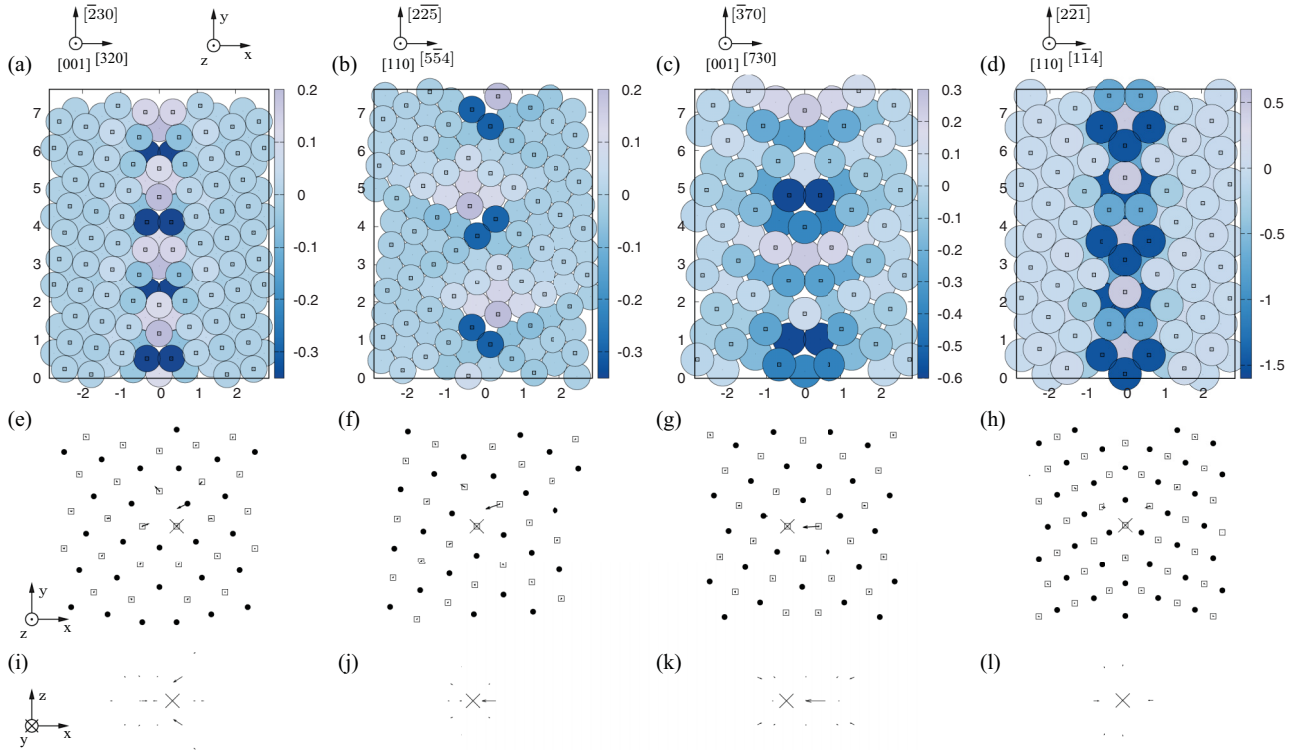


FIG. 5. Symmetrical tilt grain boundary structures without vacancies: (a)  $\Sigma 13(320)[001]$ , (b)  $\Sigma 33(554)[110]$  in Al, and (c)  $\Sigma 29(730)[001]$ , (d)  $\Sigma 9(114)[110]$  in bcc Fe. Colors represent the vacancy segregation energy ( $\Delta E_{\text{seg}}$ ). The minimum values are given in Table II. The relaxations around a single vacancy in this optimal configuration are represented by arrows in (e)–(h) projected in the  $(x, y)$  plane and in the  $(x, z)$  plane in (i)–(l) (only the displacements are shown). The vacant site is marked by a large cross.

is crucial and should be minimized. In these tests, they were selected according to the amplitude of their relaxation in the topology with a threshold that is specified by  $u_{\text{Topo}}$ . Both Nn and  $u_{\text{Topo}}$  are given in Table I. Finally, the “global” acceptance rate is also reported. In this case, the moves also involve sites that are not those of optimal segregation energy and therefore less prone to be visited. They are nonetheless important for sampling arrangements of several vacancies.

The process of finding the topologies necessary for the SD moves also produces activation barriers. Although not used in the Monte Carlo simulation, they provide interesting information concerning the kinetics of the vacancies. The effective barrier for diffusion along the tilt axis  $E_a^{\text{tilt}}$  and the

effective barrier to exit the GB  $E_a^{\text{out}}$  are given in Table II. The former is the minimum barrier for a change in the  $z$  position of the vacancy, and the latter is calculated following the minimum energy path. It is composed of several jumps and stops when the vacancy bulk activation barrier is recovered. The local minima along the path form a basin where, as a first approximation, the occupancies are considered equilibrated before the exit event [50]. The escape rate (through the path) is the product of the probability of being in the last local minimum along the path times the frequency for crossing the last barrier. If the bottom of the basin has a significantly lower energy than the others, the prefactor ahead of the final rate can be approximated. Then, the effective

TABLE I. Acceptance rates for exchange moves between equivalent sites along the tilt axis, with different types of moves: X, simple exchange; SD, Smart Darting move; SD+R+b, Smart Darting move combined with a Rosenbluth sampling of the Nn neighbors of the vacancy that have a displacement larger than  $u_{\text{Topo}}$ .  $u_{\text{max}}$  is the maximum amplitude of the relaxations. The “global” acceptance rate is also given. Numbers in parentheses are the mean-square difference obtained from four independent runs.

	$\Sigma 13$	$\Sigma 33$	$\Sigma 29$	$\Sigma 9$
SD	0.011 (0.003)	0.018 (0.001)	0.016 (0.001)	0.066 (0.004)
SD+R+b	0.046 (0.001)	0.058 (0.003)	0.030 (0.001)	0.102 (0.003)
global	0.010 (0.0002)	0.011 (0.0002)	0.005 (0.0002)	0.014 (0.0003)
X	$<6 \times 10^{-5}$	$<4 \times 10^{-5}$	$<4 \times 10^{-5}$	$<10^{-4}$
Nn	2	1	1	2
$u_{\text{max}} (a_0)$	0.23	0.30	0.40	0.11
$u_{\text{Topo}} (a_0)$	0.2	0.1	0.2	0.1



TABLE II. Bulk vacancy formation energy  $E_f^{\text{bulk}}$ , vacancy segregation energy  $\Delta E_{\text{seg}}$  on the most favorable site, energy barrier for an exchange between a vacancy and a first neighbor in a perfect crystal environment  $E_a^{\text{bulk}}$ , effective energy barrier for diffusion along the tilt axis of the GB  $E_a^{\text{tilt}}$ , and effective energy barrier to leave the GB  $E_a^{\text{out}}$ .

	$\Sigma 13$	$\Sigma 33$	$\Sigma 29$	$\Sigma 9$
$E_f^{\text{bulk}}$ (eV)	0.68	0.68	2.10	2.10
$\Delta E_{\text{seg}}$ (eV)	-0.43	-0.29	-0.64	-1.49
$E_a^{\text{bulk}}$ (eV)	0.65	0.65	0.68	0.68
$E_a^{\text{tilt}}$ (eV)	0.82	0.61	0.76	0.97
$E_a^{\text{out}}$ (eV)	0.99	0.94	1.13	2.15

energy barrier for exiting the basin is simply the difference in segregation energy between the bottom of the basin and the last state before the exit added to the last jump barrier. It is this value that is reported as the effective barrier for exiting the GB. The vacancy diffusion along the grain boundaries is found to be significantly dependent on the structure (as already known from MD simulations of self-diffusion [51]). The exit barrier is always much larger than the bulk barrier. It is close to, but not exactly equal to, the difference between the bulk activation energy and the segregation energy. In contrast, the activation energy for diffusion along the tilt axis can be larger or smaller than the bulk value, meaning that intergranular vacancies do not necessarily diffuse faster than bulk vacancies. Nevertheless, self-diffusion is faster than in the bulk because the vacancy formation energy is decreased. Finally, for these grain boundaries, the diffusion occurs along the tilt axis with no easy path to move from one structural unit to the other (i.e., in the  $y$  direction). The activation energy in the  $y$  direction can be taken, as an approximation, as the exit activation energy. The aggregation of two vacancies is also studied by the MCMC method. The goal is to demonstrate that the method can handle the simplest vacancy clusters before moving to larger clusters, under the influence of elastic strains, in connection to the fracture mechanisms mentioned in the Introduction. Each grain boundary studied exhibits a different behavior. The results of two representative simulations are reported in Fig. 6. Others, in Al and Fe, are discussed in the Supplemental Material [43]. The insets [Figs. 6(a) and 6(b)] represent the position of the vacancies along the tilt axis of the GBs along the Markov chain. Periodic boundary conditions are applied. The length of the simulation box is 12 periods in both cases, but one period is  $1a_0$  long for the  $\Sigma 13$  of axis [001] and  $\sqrt{2}/2a_0$  for the  $\Sigma 33$  of axis [110]. Therefore, the nearest crystallographically equivalent sites along the tilt axis are a second neighbor and a first neighbor, respectively. Both insets demonstrate that the  $z$  positions are well sampled. The clustering tendency is very different. In the  $\Sigma 13$  case, the distance between the vacancies ( $d$ ) fluctuates between 1 and  $L_z/2$ , which is the maximum separation allowed by the periodic boundary conditions. The energy of the topologies “visited” is superimposed to  $d$ . This energy is the one found after minimization when the topology is extracted. It is not the current energy of the system. “Visited” is to be taken in the “Smart Darting” sense, i.e., the distance between the microstate and the local energy minimum is lower than the

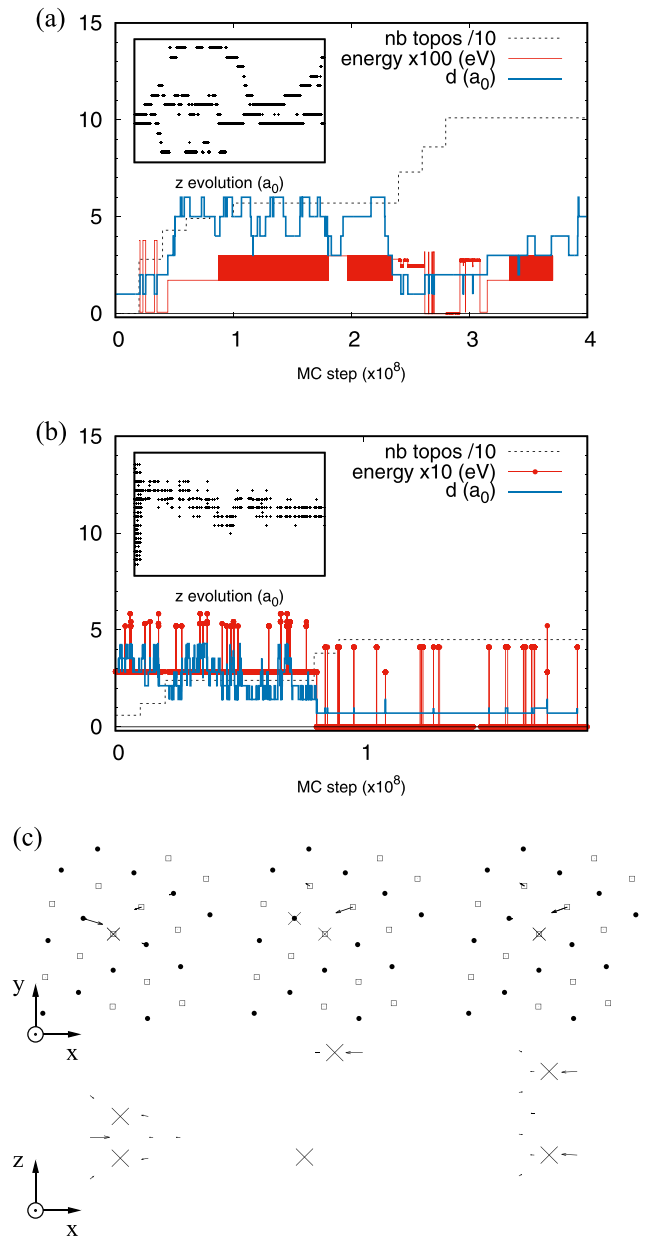


FIG. 6. Evolution of the distance between the vacancies, the energy of the topology visited, and the number of topologies detected along the Markov chain for a system containing two vacancies: (a)  $\Sigma 13(320)[001]$  at  $T = 300$  K, (b)  $\Sigma 33(554)[110]$  at  $T = 600$  K both in Al. The position in  $z$  (the tilt axis direction) is shown in the inset. (c) The three main topologies visited in (b) with energies 0, 0.52, and 0.28 eV from left to right.

threshold defining the neighborhood of the local minimum in SD. The energy variations are small, lower than 0.05 eV. The minimum energy found is a configuration where the vacancies are separated by a distance of  $2a_0$ . The saddle searches have explored configurations with  $d < 1$ , and their energies are higher than the minimum by 0.4–0.6 eV, which might explain why transitions from microstates with  $d = 1$  to those with  $d < 1$  are not observed. Therefore, for this grain boundary, the vacancies remain split. In contrast, in the  $\Sigma 33$  case, the vacancies bind. The evolution of  $d$  [Fig. 6(b)] illustrates how

the algorithm explores new configurations that enrich the list of topologies, which opens new transitions for Smart Darting, such as transitions with smaller and smaller  $d$ . The simulation is started with  $d$  maximum and the list of topologies obtained for the single vacancy. First,  $d$  fluctuates with values larger than three times the period in  $z$  until the method learns the configurations where  $d$  is equal to two periods. Then, these configurations are visited without significant energy changes, and from there, the method finds the configuration where the vacancies bind in the first-neighbor position. The energy drops by approximately 0.3 eV. Beyond this point, the energy fluctuates with an amplitude as high as 0.5 eV ( $T = 600$  K), and the cluster moves along the tilt axis, without complete splitting [see the inset in Fig. 6(b)]. The total number of topologies extracted is 45, but essentially three are visited. They are represented in Fig. 6(c). The stable divacancy configuration is intuitive: a pair of first neighbors, occupying the GB site where the segregation energy of an isolated vacancy is the lowest. Note that the relaxations are very different. It is representative of several grain boundaries. For example, in the case of Fe, the vacancies bind by more than 1 eV in  $\Sigma 29$  and form pairs along the tilt axis with a separation of one period ( $1a_0$ ). In the  $\Sigma 9$  case, they repel each other by 60 meV and therefore remain split (see the Supplemental Material [43]). It is not always the case: in the  $\Sigma 9\{221\}[110]$  in Al, there are more configurations of low energy, connected by low-energy barriers, and some of them are only different by the relaxations. The MCMC simulation handles this situation: the transitions over the low barriers by  $\Delta u$  moves and the splitting/reforming of the divacancy by Smart Darting moves. The distribution of the energy of the topologies, the structure of the low-energy divacancies, and the relevant energy barriers are given in the Supplemental Material [43].

#### IV. DISCUSSION AND CONCLUSION

One interesting question about intergranular vacancies is whether their specific structure, qualified as “delocalized,” leads to specific properties or if they behave in a similar way as in the bulk. Regarding diffusion, our findings are similar to what is summarized in the Introduction: several sites lead to the delocalized structure (the dark sites in Fig. 5), which means that long jumps can be expected when entering the GBs. In contrast, once the vacancy is in the optimum location, saddle searches have not revealed any low-energy path for diffusing out of this configuration, and the barriers are similar to bulk diffusion (Table II). The elastic field produced is analyzed by calculating the elastic dipole tensor  $P_{ij}$  (Table IV) via the Kanzaki forces [52]. Convergence of the calculation with the number of neighbor shells gives an estimate of the range of the elastic deformation produced by the defect. The influence of the number of shells restored [52,53] gives an estimate of the range of the anharmonic region around the defect. The range of the elastic field is approximately  $3a_0$ , similar to the bulk ( $r_e$  in Table IV). In contrast, the range of the anharmonic relaxations can be much larger in the GBs, up to  $1.75a_0$ . These values are coherent with the radius used for defining the topologies ( $2.5a_0$ ), which was found empirically by increasing the radius until no configuration built from the topologies relaxed toward a different minimum from the

one targeted. Furthermore, the amplitude of  $P_{ij}$  in the GBs can be approximately twice that in the bulk (Table IV). This suggests that an external elastic field could have a significant impact on the segregation energies. Indeed, the magnitude of this difference, typically 4 eV, leads to interaction energies of the same order of magnitude as the segregation energies for reasonably large elastic strains. For example, 2% normal strain  $\epsilon_{11}$  leads to  $\Delta E_e = -(P_{ij}^{\text{gb}} - P_{ij}^{\text{bulk}})\epsilon_{ij}^{\text{ext}} \sim 0.08$  eV, which is already of the order of 20% of the segregation energy (Table II). In contrast, the calculation of the vacancy-vacancy elastic interaction energy, from the  $P_{ij}$  and within isotropic elasticity (the Al case), gives a negligible interaction (on the order of 1 meV in first neighbor along the tilt axis of  $\Sigma 33$ ). The binding energies found, which are therefore pure core effects, depend on the structure and are different from the bulk values:  $-0.02$ ,  $0.3$ ,  $1$ , and  $-0.06$  eV for  $\Sigma 13$ ,  $\Sigma 33$ ,  $\Sigma 29$ , and  $\Sigma 9$ , respectively, while in the bulk the interaction is zero in Al [54] and 0.14 and 0.3 eV in the first- and second-nearest-neighbor positions in Fe [55]. Additionally, because the segregation energies are large, the interactions are along the tilt axis in every case. In brief, the differences between a bulk and a delocalized intergranular vacancy are a strong anisotropy for diffusion, which is essentially along the tilt axis, an enhanced elastic interaction with external elastic fields and a structure-dependent tendency of forming one-dimensional chains, in the four structures studied, which are pure tilt. Note that the binding is quite different in twist grain boundaries where vacancies accumulate at the intersections of screw dislocations [56].

In conclusion, the paper presents an extension of Markov chain Monte Carlo that overcomes the limitations of the vanishing acceptance rate for particle exchanges in the case of large relaxations. The method is illustrated in the particularly demanding case of delocalized intergranular vacancies. The Monte Carlo moves are composed of the classical random particle displacements and vacancy-particle exchanges, to which “Smart Darting” moves are added. They are based on a list of topologies built on the fly, which contain the relaxations around the vacancies in the configurations of local minimum potential energy. When the system enters a neighborhood of one such minimum, it can be transported in the vicinity of another minimum of the list. In the vacancy case, the move consists in erasing the relaxations of the neighbors of the vacancy before inserting a particle at its location and creating the appropriate relaxations at its new location. Taking four different tilt boundaries, it is shown that the occupancy of the crystallographically equivalent sites along the tilt axis can be sampled with acceptance rates of several % at room temperature. These high rates are obtained when, in addition to “Smart Darting,” the positions of key neighbors are also sampled. Note that if the relaxations are dilatations, a similar but simpler algorithm exists [57]. Divacancies were also studied by the method. They exhibit GB-specific behaviors such as permanent binding, dissociation followed by immediate binding, or no interaction at all. Additional data are reported that could be useful to build mesoscale models: elastic dipole tensors, activation barriers for 1D diffusion along the tilt axis, and effective barriers to exit the GB or diffuse perpendicular to the tilt axis. Future work will consist in sampling intergranular vacancy configurations beyond two vacancies

and under the influence of an external strain, since the use of particle displacements enables equilibrating stresses when applying a displacement on the side of the system. The effect of elastic strains on intergranular vacancies seems particularly strong and is important in the context of ductile fracture [1], including under irradiation [58], and in thin films [59] when discussing the existence of cavities.

### ACKNOWLEDGMENTS

This project has received funding from the Euratom research and training programme 2014-2018 under Grant Agreement No. 755039 (M4F project). A. F. Voter and D. Perez (Los Alamos National Laboratory) kindly introduced me to the Smart Darting method and k-ART during numerous visits at LANL funded by the CNRS-pics program and LANL.

### APPENDIX A: ADDITIONAL DETAILS CONCERNING THE DEFINITION AND CHOICE OF $\epsilon$

The cubes that define the  $\epsilon$ -sphere have to be compatible with the Voronoi tessellation. When the cube is not entirely contained in the Voronoi cell, the volume considered available for the neighbor in the definition of the  $\epsilon$ -sphere is the intersection of the cube of side  $2\epsilon$  and the Voronoi cell. To respect the symmetry of the MC move, this constraint on the displacement of the neighbor should be imposed also for the reverse move. In addition, the original Smart Darting move considers that the spheres do not overlap. If the vacancy arrangement is not the same between topologies, there is no constraint on the value of  $\epsilon$ , apart from the compatibility with the Voronoi tessellation, and  $\epsilon$  can be large. On the contrary, if the vacancies occupy the same sites and only the displacements are different [such as in Fig. 1(a)],  $\epsilon$  should be half of the maximum difference in displacement over the sites included in the topology. It could be a small number. The measurement of the displacement fluctuations on bulk sites shows that their maximum amplitude is of the order of  $0.1a_0$  at  $T = 300$  K. For this reason, when deciding in the “search” phase of the algorithm which state is eligible for a topology extraction, the constraint imposed is that it should be at minimum at a distance  $0.2a_0$  from an already known topology. Unfortunately, in the GB there are often displacements beyond  $0.15a_0$ , even not connected to vacancies. A small value of  $0.1a_0$  for  $\epsilon$  is therefore unpractical. The value  $\epsilon = 0.2a_0$  was chosen from the distance fluctuations in Fig. 2(b), and therefore the cubes overlap in the Voronoi cell of Fig. 1(a). It has no consequence for the simulations presented (it was checked), because this neighbor is tightly bound to the local minima, and  $\epsilon = 0.1a_0$  would work for this site, but not for the other sites of the GB. One solution, not implemented yet, would be to use site-dependent values of  $\epsilon$  in the topologies where this is needed. This is left for future work.

TABLE III. Simulation box sizes  $L_x, L_y, L_z$  ( $a_0$ ), number of atoms  $nat$ , and coincidence site lattice cell size  $CSL_x, CSL_y, CSL_z$  ( $a_0$ ).

	$\Sigma 13$	$\Sigma 33$	$\Sigma 29$	$\Sigma 9$
$L_x$ ( $a_0$ )	31.3	32.2	15.6	33.8
$L_y$ ( $a_0$ )	14.4	11.5	15.2	12.0
$L_z$ ( $a_0$ )	12.0	8.48	16	17.0
$nat$	19776	12528	7232	13632
$CSL_x$ ( $a_0$ )	7.2	8.12	7.6	8.48
$CSL_y$ ( $a_0$ )	7.2	5.74	7.6	6.0
$CSL_z$ ( $a_0$ )	1.0	0.71	1.0	1.41

### APPENDIX B: TECHNICAL DETAILS

The particles interact by EAM potentials: Ref. [42] for Al and Ref. [55] for Fe. The box sizes are given in Table III and the crystallographic directions in Fig. 5. Periodic boundary conditions are applied in the  $y$  and  $z$  directions, and two regions are fixed on the sides perpendicular to the  $x$  direction (the normal to the GBs). The width of the rigid regions is the range of the potential plus  $0.5a_0$ . The main parameters for SD are  $\epsilon = 0.2a_0$ , the size of the neighborhood around the local energy minima, the radius around the vacancy for defining the topology is  $2.5a_0$  in the plane perpendicular to the tilt axis and  $2.2a_0$  along the tilt axis, and the number of random displacements per atom in the Rosenbluth sampling  $Nr = 1000$ . Note that the displacements are taken within a cube of side  $\epsilon$ , therefore it is a dense sampling.

### APPENDIX C: ELASTIC DIPOLE TENSOR

The components for the elastic dipole tensor  $P_{ij}$  are shown in Table IV.

TABLE IV. Components of the elastic dipole tensor  $P_{ij}$  (eV) for a vacancy in bulk Al and Fe and in the four grain boundaries, in the favorable configuration (Fig. 5), computed from the Kanzaki forces [52]. The range of the elastic distortions  $r_e$  and of the anharmonicity  $r_a$  are also given ( $a_0$ ).

	Bulk Al	$\Sigma 13$	$\Sigma 33$	Bulk Fe	$\Sigma 29$	$\Sigma 9$
$P_{11}$ (eV)	-3.9	-11.2	-7.5	-1.3	-21.0	-7.8
$P_{22}$ (eV)	-3.9	-8.8	-3.3	-1.3	-4.0	-8.2
$P_{33}$ (eV)	-3.9	-4.5	-7.2	-1.3	-11.8	-7.1
$P_{12}$ (eV)	0.0	-4.0	-2.3	0.0	-0.3	0.0
$P_{13}$ (eV)	0.0	0.0	0.0	0.0	0.0	0.0
$P_{23}$ (eV)	0.0	0.0	0.0	0.0	0.0	0.0
$P_{11}$ (eV)	-2.5 <sup>a</sup>			-3.6 <sup>b</sup>		
$r_e$ ( $a_0$ )	2.5-3.0	3.0	3.0	3.5	3.5	3.5
$r_a$ ( $a_0$ )	0.7	1.58	1.75	1.41	1.75	1.75

<sup>a</sup>DFT value from Ref. [60].

<sup>b</sup>DFT value from Ref. [61].

- [1] P. J. Noell, R. Sills, A. A. Benzerga, and B. L. Boyce, Void nucleation during ductile rupture of metals: A review, *Prog. Mater. Sci.* **135**, 101085 (2023).
- [2] P. J. Noell, J. E. Sabisch, D. L. Medlin, and B. L. Boyce, Nanoscale conditions for ductile void nucleation in copper: Vacancy condensation and the growth-limited microstructural state, *Acta Mater.* **184**, 211 (2020).
- [3] P. Lukáš, L. Kunz, L. Navrátilová, and O. Bokůvka, Fatigue damage of ultrafine-grain copper in very-high cycle fatigue region, *Mater. Sci. Eng. A* **528**, 7036 (2011).
- [4] T. Miura, K. Fujii, and K. Fukuya, Micro-mechanical investigation for effects of helium on grain boundary fracture of austenitic stainless steel, *J. Nucl. Mater.* **457**, 279 (2015).
- [5] D. Tanguy, Cohesive stress heterogeneities and the transition from intrinsic ductility to brittleness, *Phys. Rev. B* **96**, 174115 (2017).
- [6] G. M. Scamans, R. Alani, and P. R. Swann, Pre-exposure embrittlement and stress corrosion failure in AlZnMg alloys, *Corros. Sci.* **16**, 443 (1976).
- [7] M. L. Martin, B. P. Somerday, R. O. Ritchie, P. Sofronis, and I. M. Robertson, Hydrogen-induced intergranular failure in nickel revisited, *Acta Mater.* **60**, 2739 (2012).
- [8] I. M. Robertson, P. Sofronis, A. Nagao, M. Martin, S. Wang, D. Gross, and K. Nygren, Hydrogen embrittlement understood, *Metall. Mater. Trans. A* **46**, 2323 (2015).
- [9] M. L. Martin, I. M. Robertson, and P. Sofronis, Interpreting hydrogen-induced fracture surfaces in terms of deformation processes: A new approach, *Acta Mater.* **59**, 3680 (2011).
- [10] J. Huang, M. Meyer, and V. Pontikis, Is pipe diffusion in metals vacancy controlled? A Molecular-Dynamics study of an edge dislocation in copper, *Phys. Rev. Lett.* **63**, 628 (1989).
- [11] J. von Boehm and R. M. Nieminen, Molecular-dynamics study of partial edge dislocations in copper and gold: Interactions, structures, and self-diffusion, *Phys. Rev. B* **53**, 8956 (1996).
- [12] Q. F. Fang and R. Wang, Atomistic simulation of the atomic structure and diffusion within the core region of an edge dislocation in aluminum, *Phys. Rev. B* **62**, 9317 (2000).
- [13] A. Suzuki and Y. Mishin, Atomic mechanisms of grain boundary diffusion: Low versus high temperatures, *J. Mater. Sci.* **40**, 3155 (2005).
- [14] A. Suzuki and Y. Mishin, Interaction of point defects with grain boundaries in fcc metals, *Interface Sci.* **11**, 425 (2003).
- [15] A. Suzuki and Y. Mishin, Atomistic modeling of point defects and diffusion in copper grain boundaries, *Interface Sci.* **11**, 131 (2003).
- [16] M. R. Sørensen, Y. Mishin, and A. F. Voter, Diffusion mechanisms in Cu grain boundaries, *Phys. Rev. B* **62**, 3658 (2000).
- [17] H. Zhang, D. J. Srolovitz, J. F. Douglas, and J. A. Warren, Atomic motion during the migration of general [001] tilt grain boundaries in Ni, *Acta Mater.* **55**, 4527 (2007).
- [18] H. Zhang, D. J. Srolovitz, J. F. Douglas, and J. A. Warren, Characterization of atomic motion governing grain boundary migration, *Phys. Rev. B* **74**, 115404 (2006).
- [19] T. Frolov, D. L. Olmsted, M. Asta, and Y. Mishin, Structural phase transformations in metallic grain boundaries, *Nat. Commun.* **4**, 1899 (2013).
- [20] A. P. Sutton and R. W. Balluffi, *Interfaces in Crystalline Materials* (Oxford Science, Oxford, 1995).
- [21] J. Han, V. Vitek, and D. J. Srolovitz, The grain-boundary structural unit model redux, *Acta Mater.* **133**, 186 (2017).
- [22] J. Han, V. Vitek, and D. J. Srolovitz, Grain-boundary metastability and its statistical properties, *Acta Mater.* **104**, 259 (2016).
- [23] W. Han, M. Demkowicz, E. Fu, Y. Wang, and A. Misra, Effect of grain boundary character on sink efficiency, *Acta Mater.* **60**, 6341 (2012).
- [24] J. Han, V. Vitek, and D. J. Srolovitz, The interplay between grain boundary structure and defect sink/annealing behavior, *IOP Conf. Ser.: Mater. Sci. Eng.* **89**, 012004 (2015).
- [25] K. Kolluri and M. J. Demkowicz, Formation, migration, and clustering of delocalized vacancies and interstitials at a solid-state semicoherent interface, *Phys. Rev. B* **85**, 205416 (2012).
- [26] W. S. Yu and M. J. Demkowicz, Non-coherent Cu grain boundaries driven by continuous vacancy loading, *J. Mater. Sci.* **50**, 4047 (2015).
- [27] W. Jäger and H. Trinhaus, Defect ordering in metals under irradiation, *J. Nucl. Mater.* **205**, 394 (1993).
- [28] Y. Gao, Y. Zhang, D. Schwen, C. Jiang, C. Sun, J. Gan, and X.-M. Bai, Theoretical prediction and atomic kinetic Monte Carlo simulations of void superlattice self-organization under irradiation, *Sci. Rep.* **8**, 6629 (2018).
- [29] R. J. Zamora, B. P. Uberuaga, D. Perez, and A. F. Voter, The modern temperature-accelerated dynamics approach, *Annu. Rev. Chem. Biomol. Eng.* **7**, 87 (2016).
- [30] D. Perez, E. D. Cubuk, A. Waterland, E. Kaxiras, and A. F. Voter, Long-time dynamics through parallel trajectory splicing, *J. Chem. Theory Comput.* **12**, 18 (2016).
- [31] G. Henkelman and H. Jónsson, Long time scale kinetic monte carlo simulations without lattice approximation and predefined event table, *J. Chem. Phys.* **115**, 9657 (2001).
- [32] L. K. Béland, P. Brommer, F. El-Mellouhi, J.-F. Joly, and N. Mousseau, Kinetic activation-relaxation technique, *Phys. Rev. E* **84**, 046704 (2011).
- [33] R. B. Garza, J. Lee, M. H. Nguyen, A. Garmon, D. Perez, M. Li, J. C. Yang, G. Henkelman, and W. A. Saidi, Atomistic mechanisms of binary alloy surface segregation from nanoseconds to seconds using accelerated dynamics, *J. Chem. Theory Comput.* **18**, 4447 (2022).
- [34] D. Frenkel and B. Smit, *Understanding Molecular Simulation*, 2nd ed. (Academic Press, San Diego, 2002).
- [35] A. Seki, D. N. Seidman, Y. Oh, and S. M. Foiles, Monte carlo simulations of segregation at [001] twist boundaries in a Pt(Au) alloy-I: results, *Acta Metall. Mater.* **39**, 3167 (1991).
- [36] R. K. Koju and Y. Mishin, Relationship between grain boundary segregation and grain boundary diffusion in Cu-Ag alloys, *Phys. Rev. Mater.* **4**, 073403 (2020).
- [37] I. Andricioaei, J. E. Straub, and A. F. Voter, Smart darting Monte Carlo, *J. Chem. Phys.* **114**, 6994 (2001).
- [38] S. M. Foiles, Calculation of the surface segregation of Ni-Cu alloys with the use of the embedded-atom method, *Phys. Rev. B* **32**, 7685 (1985).
- [39] D. Tanguy and M. Mareschal, Superabundant vacancies in a metal-hydrogen system: Monte carlo simulations, *Phys. Rev. B* **72**, 174116 (2005).
- [40] E. Vamvakopoulos and D. Tanguy, Equilibrium vacancy concentrations in Al- $\Sigma=33(554)[110]$  by grand canonical Monte Carlo simulations, *Phys. Rev. B* **79**, 094116 (2009).
- [41] C. H. Rycroft, A three-dimensional Voronoi cell library in C++, *Chaos* **19**, 041111 (2009).

- [42] Y. Mishin, D. Farkas, M. J. Mehl, and D. A. Papaconstantopoulos, Interatomic potentials for monatomic metals from experimental data and ab initio calculations, *Phys. Rev. B* **59**, 3393 (1999).
- [43] See Supplemental Material at <http://link.aps.org/supplemental/10.1103/PhysRevMaterials.8.033604> for additional details on vacancy trajectories, segregation energy profiles, additional simulations in Fe and Al, as well as the convergence of the calculation of the elastic dipole tensor.
- [44] H. Jónsson, G. Mills, and K. Jacobsen, *Classical and Quantum Dynamics in Condensed Phase Simulations* (World Scientific, Singapore, 1998), p. 385.
- [45] D. Frenkel, G. C. A. M. Mooij, and B. Smit, Novel scheme to study structural and thermal properties of continuously deformable molecules, *J. Phys.: Condens. Matter* **4**, 3053 (1992).
- [46] J. D. Rittner and D. N. Seidman, [110] symmetric tilt grain-boundary structures in fcc metals with low stacking-fault energies, *Phys. Rev. B* **54**, 6999 (1996).
- [47] Y. Mishin, A. Suzuki, B. P. Uberuaga, and A. F. Voter, Stick-slip behavior of grain boundaries studied by accelerated molecular dynamics, *Phys. Rev. B* **75**, 224101 (2007).
- [48] A. Rajabzadeh, F. Momprou, M. Legros, and N. Combe, Elementary mechanisms of shear-coupled grain boundary migration, *Phys. Rev. Lett.* **110**, 265507 (2013).
- [49] M. A. Tschopp, K. N. Solanki, F. Gao, X. Sun, M. A. Khaleel, and M. F. Horstemeyer, Probing grain boundary sink strength at the nanoscale: Energetics and length scales of vacancy and interstitial absorption by grain boundaries in  $\alpha$ -Fe, *Phys. Rev. B* **85**, 064108 (2012).
- [50] B. Puchala, M. L. Falk, and K. Garikipati, An energy basin finding algorithm for kinetic Monte Carlo acceleration, *J. Chem. Phys.* **132**, 134104 (2010).
- [51] Y. Mishin, M. Asta, and J. Li, Atomistic modeling of interfaces and their impact on microstructure and properties, *Acta Mater.* **58**, 1117 (2010).
- [52] E. Clouet, C. Varvenne, and T. Jourdan, Elastic modeling of point-defects and their interaction, *Comput. Mater. Sci.* **147**, 49 (2018).
- [53] G. Simonelli, R. Pasianot, and E. J. Savino, Point-defect computer simulation including angular forces in bcc iron, *Phys. Rev. B* **50**, 727 (1994).
- [54] H. Wang, D. Rodney, D. Xu, R. Yang, and P. Veyssi re, Pentavacancy as the key nucleus for vacancy clustering in aluminum, *Phys. Rev. B* **84**, 220103(R) (2011).
- [55] L. Malerba, M. Marinica, N. Anento, C. Bj rkas, H. Nguyen, C. Domain, F. Djurabekova, P. Olsson, K. Nordlund, A. Serra, D. Terentyev, F. Willaime, and C. Becquart, Comparison of empirical interatomic potentials for iron applied to radiation damage studies, *J. Nucl. Mater.* **406**, 19 (2010).
- [56] E. Mart nez and A. Caro, Atomistic modeling of long-term evolution of twist boundaries under vacancy supersaturation, *Phys. Rev. B* **86**, 214109 (2012).
- [57] H. B. Lee, F. B. Prinz, and W. Cai, Atomistic simulations of surface segregation of defects in solid oxide electrolytes, *Acta Mater.* **58**, 2197 (2010).
- [58] L. Malerba *et al.*, Multiscale modelling for fusion and fission materials: The M4F project, *Nucl. Mater. Energy* **29**, 101051 (2021).
- [59] S. Curiotto, A. Chame, P. M ller, C. V. Thompson, and O. Pierre-Louis, Hole opening from growing interfacial voids: A possible mechanism of solid state dewetting, *Appl. Phys. Lett.* **120**, 091603 (2022).
- [60] D. Da Fonseca, F. Onimus, F. Momprou, M.-C. Marinica, E. de Sonis, E. Clouet, and T. Jourdan, Numerical investigation of dislocation climb under stress and irradiation, *Acta Mater.* **242**, 118431 (2023).
- [61] J. S. Wr bel, M. R. Zemla, D. Nguyen-Manh, P. Olsson, L. Messina, C. Domain, T. Wejrzanowski, and S. L. Dudarev, Elastic dipole tensors and relaxation volumes of point defects in concentrated random magnetic Fe-Cr alloys, *Comput. Mater. Sci.* **194**, 110435 (2021).